

We are IntechOpen, the world's leading publisher of Open Access books Built by scientists, for scientists

6,900

Open access books available

185,000

International authors and editors

200M

Downloads

Our authors are among the

154

Countries delivered to

TOP 1%

most cited scientists

12.2%

Contributors from top 500 universities



WEB OF SCIENCE™

Selection of our books indexed in the Book Citation Index
in Web of Science™ Core Collection (BKCI)

Interested in publishing with us?
Contact book.department@intechopen.com

Numbers displayed above are based on latest data collected.
For more information visit www.intechopen.com



Resistance to Corrosion and Passivity of 316L Stainless Steel Directionally Solidified Samples

Claudia Marcela Méndez,
Mónica Mariela Covinich and Alicia Esther Ares

Additional information is available at the end of the chapter

<http://dx.doi.org/10.5772/57275>

1. Introduction

The three main types of crystalline structure that stainless steel can be classified are Austenitic, Ferritic and Martensitic. Austenite, also known as gamma phase iron (γ -Fe), is a metallic, non-magnetic allotrope of iron or a solid solution of iron, with an alloying element.

Ferrite, also known as α -ferrite (α -Fe) or alpha iron is a materials science term for pure iron, with a body-centered cubic crystal structure. It is this crystalline structure which gives steel and cast iron their magnetic properties. Martensite most commonly refers to a very hard form of steel crystalline structure, but it can also refer to any crystal structure that is formed by displacive transformation (Lambers et. al., 2009 and Batra et al., 2003).

These are alloys containing chromium and nickel (sometimes manganese and nitrogen), structured around the type 302 composition of iron, 18%Cr, and 8%Ni. Austenitic steels are not hardenable by heat treatment. The most familiar stainless steel is probably type 304, sometimes called T304 or simply 304. Type 304 surgical stainless steel is austenitic steel containing 18-20%Cr and 8-10%Ni (Kilicli & Erdogan, 2008).

Primary stainless steel used in aviation construction. Chemical and steel industry applicable grades are 308, 308L, 316, 316L, 316LN Nitrogen bearing, 312, 309L, 310L L denotes carbon percentage less than 0.03%, mostly used for corrosion heat resistance have work hardening properties, welding primarily done by TIG and MMAW process. Another grade, 312 is used for dissimilar steel welding, also known as universal alloy steel as unknown composition steels can be welded. For high temperature application, above 600 °C, 309 and 310 grades are preferred.

According to previous studies in the literature, there are eight separate types of corrosion, with only a few having a major impact on stainless steel (DOD Technical Bulletin – Corrosion Prevention and Detection):

1. General corrosion, this type of corrosion occurs when there is an overall breakdown of the passive film. The entire surface of the metal will show a uniform sponge like appearance. Halogens penetrate the passive film of stainless and allow corrosion to occur. Fluorine, chlorine, bromine, iodine and astatine are some of the most active.
2. Crevice corrosion, this is a problem with stainless fasteners used in seawater applications, because of the low pH of salt water.
3. Pitting, Stainless that had its passivation penetrated in a small spot becomes an anodic, with the passivated part remaining cathodic, causing pit type corrosion.
4. Galvanic corrosion, the current flows from the anodic towards the cathodic metal, and in the process slowly removes material from the anodic metal. Seawater makes a good electrolyte, and thus, galvanic corrosion is a common problem in this environment.
5. Intergranular corrosion, all austenitic stainless steels contain a small amount of carbon. At extremely high temperature, such as welding, the carbon forces local chrome to form chromium carbide around it, thus starving adjacent areas of the chrome it needs for its own corrosion protection.
6. Selective leaching, fluids will remove metal during a de-ionization or de-mineralization process. This usually happens inside a pipe and is rarely a fastener problem.
7. Erosion corrosion, this corrosion happens when the velocity of an abrasive fluid removes the passivation from a stainless. This is almost exclusively limited to pipe interiors.
8. Stress corrosion, also called stress corrosion cracking or chloride stress corrosion. Chlorides are probably the single biggest enemy of stainless steel. Next to water, chloride is the most common chemical found in nature. In most environments, the PPM are so small the effects on stainless are minute. But in extreme environments, such as indoor swimming pools, the effects can be extreme and potentially dangerous. If a stainless part is under tensile stress, the pitting mentioned above will deepen, and cracking may take place. If stainless steel bolts are used under tensile stress, in an environment where chlorine corrosion is likely, the potential for stress corrosion cracking should be examine carefully.

Hamdy et al. in 2006 realized the electrochemical impedance spectroscopy study of the corrosion behavior of some Niobium bearing Stainless Steels in 3.5% NaCl, concluding that according to EIS measurements, increasing Nb content results in increasing the localized corrosion resistance of austenitic stainless steels in NaCl. Determined that cold deformation has a critical rule on the corrosion resistance of stainless steel. The corrosion resistance increased by increasing CD up to 23%. The best localized corrosion resistance was obtained from the alloy containing 1.24% Nb and 23% cold deformation.

Pardo et al. in 2008 attempts to provide a further understanding of the effect of Mo and Mn additions on the corrosion resistance of two austenitic stainless steels, AISI 304 and 316, in 30

wt.% H_2SO_4 , concluding that the general corrosion resistance of stainless steels in 30 wt.% H_2SO_4 increased with the addition of molybdenum as an alloy element, in such a way that the corrosion current density was one order of magnitude lower than for stainless steels with low molybdenum content.

Meanwhile, manganese addition did not have any significant effect on the behaviour of the stainless steels in acid medium. Manganese does not have a significant influence on the corrosion resistance of the stainless steels, due to the little trend to form insoluble compounds in acid medium.

Azuma et al. in 2004 analyzed the crevice corrosion behaviour of stainless steels containing 25 mass% Cr, 3 mass% Mo and various amounts of Ni in natural seawater. The results showed that ferritic steels containing nickel were more resistant to corrosion than both ferritic steels without nickel and austenitic steels. The superiority of the Ni bearing ferritic steel over the other steels was in close agreement with the depassivation pH of those steels in acidic chloride solutions. The results showed that the addition of Ni to ferritic steel was effective in decreasing the depassivation pH and the dissolution rate in acidic chloride solutions at crevices.

Passive films were grown in potentiodynamic mode, by cyclic voltammetry on AISI 316 and AISI 304 stainless steels by Freire et al, 2012. The composition of these films was investigated by X-ray photoelectron spectroscopy (XPS). The electrochemical behaviour and the chemical composition of the passive films formed by cyclic voltammetry were compared to those of films grown under natural conditions (by immersion at open circuit potential, OCP) in alkaline solutions simulating concrete. The study included the effect of pH of the electrolyte and the effect of the presence of chloride ions. The XPS results revealed important changes in the passive film composition, which becomes enriched in chromium and depleted in magnetite as the pH decreases.

On the other hand, the presence of chlorides promotes a more oxidised passive layer. The XPS results also showed relevant differences on the composition of the oxide layers for the films formed under cyclic voltammetry and/or under OCP.

Khalfallah et al. in 2011 investigated the surface modification of AISI316 stainless steel by laser melting was investigated experimentally using 2 and 4 kW laser power emitted from a continuous wave CO_2 laser at different specimen scanning speeds ranged from 300 to 1500 mm/min. Also, an investigation is reported of the introduction of carbon into the same material by means of laser surface alloying, which involves pre-coating the specimen surfaces with graphite powder followed by laser melting.

The aim of these treatments was to enhance corrosion resistance by the rapid solidification associated with laser melting and also to increase surface hardness without affecting the bulk properties by increasing the carbon concentration near the surface. Different metallurgical techniques such as optical microscopy, scanning electron microscopy (SEM), and X-ray diffraction (XRD) were used to characterize the microstructure of the treated zone. The microstructures of the laser melted zones exhibited a dendritic morphology with a very fine scale with a slight increase in hardness from 200 to 230 Hv. However, the laser alloyed samples

with carbon showed microstructure consisting of γ dendrite surrounded by a network of eutectic structures (γ + carbide). A significant increase in hardness from 200 to 500 Hv is obtained. Corrosion resistance was improved after laser melting, especially in the samples processed at high laser power (4 kW). There was shift in I_{corr} and E_{corr} toward more noble values and a lower passive current density than that of the untreated materials. These improvements in corrosion resistance were attributed to the fine and homogeneous dendritic structure, which was found throughout the melted zones. The corrosion resistance of the carburized sample was lower than the laser melted sample.

Liou et al., 2002, studied the effects of nitrogen content and the cooling rate on the reformation of austenite in the Gleeble simulated heat-affected zone (HAZ) of 2205 duplex stainless steels (DSSs). The variation of stress corrosion cracking (SCC) behavior in the HAZ of 40 wt%CaCl₂ solution at 100°C was also studied. Grain boundary austenite (GBA), Widmanstätten austenite (WA), intergranular austenite (IGA) and partially transformed austenite (PTA) were present in the HAZ. The types and amounts of these reformed austenites varied with the cooling rate and nitrogen content in the DSS. U-bend tests revealed that pitting corrosion and selective dissolution might assist the crack initiation, while the types and amounts of reformed austenite in the HAZ affected the mode of crack propagation.

The presence of GBA was found to promote the occurrence of intergranular stress corrosion cracking. WA, IGA and PTA were found to exhibit a beneficial effect on SCC resistance by deviating the crack propagation path.

Mottu et al. in 2004 studied 316LVM, coldworked austenitic stainless steel, was implanted at 49 keV with molybdenum ions. Implantation doses varied between 1×10^{15} and 3.5×10^{16} ions cm^{-2} . The structure of the implanted layer was examined by grazing incidence X-ray diffraction and the chemical composition was characterized by X-ray photoelectron spectroscopy combined with argon sputtering. Pitting corrosion studies were carried out on both unimplanted and implanted stainless steels in neutral chloride medium. The relationship between the pitting corrosion resistance, the structural and chemical modifications induced by Mo implantation was discussed. As a function of molybdenum ion dose, an expansion of fcc austenite was first observed, then above 8×10^{15} ions cm^{-2} a new bcc structure appeared and finally the implanted layer was partially amorphized. Electrochemical studies revealed that ion implantation enhances the pitting corrosion resistance. Increase in molybdenum implantation dose was beneficial up to 8×10^{15} ions cm^{-2} in improving the pitting corrosion resistance, beyond which it had a detrimental effect.

Freire et al., 2009, studied iron oxide thin layers formed on mild steel substrates in alkaline media by the application of different anodic potentials were studied in order to characterize their morphology, composition and electrochemical behaviour, in particular under conditions of cathodic protection. The surface composition was evaluated by X-Ray Photoelectron Spectroscopy (XPS) and Auger Electron Spectroscopy (AES). The morphology of the surface oxides was studied via Atomic Force Microscopy (AFM). The electrochemical behaviour of the surface oxides was studied using Electrochemical Impedance Spectroscopy (EIS). The results showed that the surface film is composed by Fe^{2+} oxides and Fe^{3+} oxides and/or hydroxides. The contribution of Fe^{2+} species vanishes when the potential of film formation increases in the

passive domain. Two distinct phases were differentiated in the outer layers of the surface film, which proves that film growing is topotactic in nature.

Park and Kwon examined the effects of Mn on the localized corrosion, anodic dissolution behavior, and repassivation kinetics of Fe–18Cr–xMn (x = 0, 6, 12) alloys using potentiodynamic tests with or without microelectrochemical cell, electrochemical impedance spectroscopy (EIS), and rapid scratch electrode tests. The addition of Mn to Fe–18Cr alloy significantly degrades passivity by decreasing the resistance to localized corrosion, and also by expanding the active region in the noble direction. The decrease in the resistance to localized corrosion of the alloys is due primarily to an increase in the number and size of Mn-containing oxides, acting as initiation sites for pitting corrosion. It was demonstrated using a micro-electrochemical test that the inherent protectiveness of passive film is also considerably reduced by the Mn addition, even though the deleterious influences of Mn-containing oxides are completely excluded. Mn facilitates the metal dissolution reaction by enhancing the activity of iron adsorbed intermediate or by generating second intermediate species (possibly manganese adsorbed intermediate) acting as another dissolution path. Further, the Mn addition appears to suppress the passivation process by reducing the activity of Cr-adsorbed species in an acidic solution, and hence the repassivation rate is significantly decreased with Mn content of the alloys.

Machuca et al., 2012 conducted measurements to evaluate localized corrosion on UNS S31603, UNS S31803, UNS S32750, UNS S31254 and UNS N08825 in natural seawater. Critical pitting and crevice temperatures were assessed using a potentiostatic technique and critical potentials for pitting and crevice corrosion initiation and repassivation were identified using potentiodynamic polarization at temperatures from 5 to 40 °C. Passivity breakdown always occurred through pitting and crevice growth above a transition temperature. Below this temperature, pitting corrosion was not observed on any of the alloys regardless of the applied potential, but initiation of crevice corrosion occurred after the alloys reached a transpassive potential.

The summary of main results about corrosion behaviour and passivity of stainless steels can be seen in Table 1.

Date	Authors	Summary of main results
2001	Ilevbare, G.O. ; Burstein, G.T.	The presence of Mo assists the rapid repassivation of the bare metal so that further metal dissolution and, therefore, metastable pit formation is prevented.
2002	Polo, J.L. ; Cano, E.; Bastidas, J.M.	A depressed capacitive loop at high frequencies indicating a charge transfer process; a second capacitive loop at intermediate frequencies attributed to adsorption_/desorption processes; and a third capacitive response at low frequencies associated with a diffusion process through corrosion products inside pits.
2002	Liou, H.Y.; Hsieh, R.I.; Tsai, W.T.	The presence of Widmanstatten, intergranular austenite and partially transformed austenite exhibited beneficial effect on SCC resistance by deviating the crack propagation path.

Date	Authors	Summary of main results
2004	Azuma, S. ; Kudo, T.; Miyuki, H. ; Yamashita, M.; Uchida, H.	Crevice corrosion behaviours of stainless steels containing 25% Cr, 3% Mo and various amounts of Ni were investigated by immersion tests in natural seawater and in a 10% ferric chloride solution. In the seawater immersion, 4% Ni ferritic steel showed higher resistance than 0% Ni ferritic steel and 30% Ni austenitic steel. In contrast, the CCT in 10% ferric chloride solution was steadily decreased with increasing the Ni content.
2005	Mottu, N. ; Vayer, M. ; Dudognon, J. ; Erre, R.	Improvement of the repassivation of the passive layer observed in this group has to be related to the increase of Mo concentration in the passive layer.
2006	Hamdy, A.S.; El-Shenawy, E. ; El-Bitar, T.	Increasing Nb content results in increasing the localized corrosion resistance of austenitic stainless steels in NaCl. Cold deformation (CD) has a critical rule on the corrosion resistance of stainless steel.
2008	Pisareka, M.; Kędzierzawskib, P.; Płociński, T.; Janik-Czachor, M.; Kurzydłowski, K.J.	The MnS inclusions do not undergo passivation; thus a large density of locations susceptible to pitting attack in a chloride-containing environment is available.
2008	Pardo, A. ; Merino, M.C. ; Coy, A.E. ; Viejo, F.; Arrabal, R. ; Matykina, E.	Molybdenum seems to play, therefore, a dual role in the improvement of the general corrosion resistance of the stainless steels by modification of passive film composition and modification of active dissolution by formation of insoluble oxides.
2008	Al-Fozan, S.A.; Malik, A.U.	The carbon steels 304 SS and 316L SS have been markedly affected by water line corrosion.
2009	Freire, L.; Nóvoa, X.R. ; Montemor, M.F. ; Carmezim, M.J.	The structure of the passive film is potential dependent and affects the efficiency of the cathodic protection current.
2010	Park, K.; Kwon, H.	The repassivation rate of Fe–18Cr–xMn (x = 0, 6, 12) was significantly reduced with Mn content. The susceptibility to metastable pitting corrosion was significantly increased with Mn content.
2010	Cai, B.; Liu, Y.; Tian, X.; Wang, F.; Li, H.; Ji, R.	Three regions, namely, the passive, active (consisting of severely attacked, commonly attacked and lightly attacked regions) and variable regions, can be observed on most crevice corrosion sites.
2011	Khalfallah, I.Y.; Rahoma, M.N.; Abboud, J.H. ; Benyounis, K.Y.	The microhardness was not increased after melting treatment but corrosion resistance improved especially when a high power is used. There was a shift in I_{corr} toward lower and nobler values after this treatment.
2012	Freire, L. ; Catarino, M.A. ; Godinho, M.I. ; Ferreira, M.J. ; Ferreira, M.G.S. ; Simoes, A.M.P.; Montemor, M.F.	The films formed on AISI 316 under d.c. potentiodynamic polarization are thicker, since the metallic contribution was hardly or even could not be detected. Moreover, the outer layers of the cycled films are extremely rich in Fe ³⁺ oxides and depleted in Fe ²⁺ , chromium oxides and nickel oxides.
2012	Machuca, L.L. ; Bailey, S.I. ; Gubner, R.	The evaluation of marine crevice corrosion mainly through the investigation of repassivation potentials is the best approach to characterize the resistance of the alloys to localized corrosion.

Table 1. Principal results about corrosion studies of stainless steels.

In the directional solidification process, the molten metal at the bottom of the mold (near to the cooling system) begins to cool and solidify before the rest of the mold does. As the metal on the bottom of the mold cools, this front of solidification moves steadily upward. By controlling the rate of flow for the molten metal feed and introducing thermal variations in the mold, shrink defects can be eliminated.

Directional solidification and progressive solidification describe types of solidification within castings. Directional solidification describes solidification that occurs from farthest end of the casting and works its way towards the sprue. Progressive solidification, also known as parallel solidification (Stefanescu, 2008), is solidification that starts at the walls of the casting and progresses perpendicularly from that surface (Chastain, 2004).

Directional solidification can be used as a purification process. Since most impurities will be more soluble in the liquid than in the solid phase during solidification, impurities will be "pushed" by the solidification front, causing much of the finished casting to have a lower concentration of impurities than the feedstock material, while the last solidified metal will be enriched with impurities.

The development of crystallographic texture during directional solidification has been analysed quantitatively in columnar castings of the Ni-base superalloys, CMSX4 and CM186LC, produced with a range of cooling rates (Ardakani, 2000).

Since directional solidification technique was firstly used to prepare turbine blade in 1960's, research work has provided an in-deep understanding of relationship of alloys, geometry, microstructure, and process conditions, the application of this knowledge to industry has proven to be challenging at best. Until now, directional solidification technique becomes more and more important research area and active technology in the field of materials science and engineering.

Directional solidification technology is also an important research instrumentally to study solidification theory. Because directional solidification can achieve controllable cooling rate with a broad range, solidification structure from near-equilibrium to far-from equilibrium condition can be obtained. A series of scientific phenomena such as interface evolution, crystal growth instability, solute redistribution, and phase selection during the course have received significant attention in recent years.

Columnar-to-equiaxed transition (CET) is one possible event in casting process. This occurs during columnar growth, usually during directional solidification, when equiaxed grains begin to form, grow, and subsequently stop the columnar growth. Normally either a columnar or equiaxed grain structures desired in industry applications, so that consistent mechanical properties are achieved throughout the casting (Gäumann et al., 2001, McFadden et al., 2009, Reinhart et al., 2005, Spittle, 2006 and Ares et al., 2000, 2002, 2007, 2010).

The CET has been examined in different type of alloys because of the advantages offered by equiaxed grain solidification. In commercial practice, attempts are made to produce either wholly columnar structures (the production of directionally solidified turbine blades) or wholly equiaxed structures. Interest in the CET therefore stems from the wish to theoretically

understand the solidification conditions that define the transition between these two extremes of structures.

In previous research, the authors of this work carried out experiments in which the conditions of columnar to equiaxed transition (CET) in directional solidification of dendritic alloys were determined. The alloy systems in this work include Pb–Sn (Ares & Schvezov, 2000), Al–Cu (Ares et al., 2011), Al–Mg (Ares et al., 2003), Al–Zn and Zn–Al alloys (Ares & Schvezov, 2007).

This work aims to study the overall influence of the variation of the structure (equiaxed, columnar and columnar-to-equiaxed transition, CET) on the corrosion resistance of 316 stainless steel in aqueous 3% NaCl (pH = 5.5) using cyclic potentiodynamic polarization techniques and electrochemical impedance spectroscopy (EIS) and investigate the relationship between the corrosion resistance of material and the secondary dendritic spacing evolution.

2. Directional solidification and structures

The alloys were prepared from pure materials of different grades, and the samples were solidified directionally upwards in a furnace which was described elsewhere (Ares et al., 2000, 2007, 2010). The temperature measurements were performed using K-type thermocouples which were protected with ceramic shields and connected to a data acquisition system controlled by a computer.

The thermocouples were previously calibrated using different temperature points: demineralized water at the freezing and boiling points (corrected by atmospheric pressure) and Fe (99.999 wt%) and Stainless Steel (99.999 wt%) at their melting points. The accuracy of thermocouples was determined to be between ± 0.25 K. The samples were melted in alumina molds of 23 mm i.d. and 25 mm e.d., with a flat bottom and a cylindrical uniform section of 200 mm high.

Five thermocouples were positioned at 20 mm intervals on the centerline of the cylinder mould from the bottom surface of the mould. During a solidification experiment, the temperature measured by each thermocouple was recorded at regular intervals of time.

Different intervals were previously tested, and as a result of this exercise, an interval of 1 second was selected. For the data processing, the readings made every 0.10 seconds during 1 second were averaged, and this value was associated to the middle of the averaged interval.

This procedure was chosen as a result of a compromise between memory available in the data logger, the time taken for an entire solidification experiment, and the degree of precision to capture the main phenomena occurring during the columnar to equiaxed transition.

The experimental procedure was as follows. At first, the liquid metal into the mould in the furnace was allowed to reach the selected temperature. Once a uniform temperature was reached, less than 1 K of difference registered between the five thermocouples located at different position in the melt, the furnace power was turned off and the melt was allowed to solidify from the bottom. Heat was extracted through a cooling system, which consisted on a copper disk attached to a copper coil, both cooled by running water. The solidification velocity

was adjusted by changing the temperature and flow of water and also by adding plates of materials between the copper plate and the crucible which changed the effective value of the thermal conductivity.

The crucible was also isolated on the top to reduced heat losses from the top of the furnace to a minimum. Temperature data acquisition was started approximately at the same time that the furnace power was turned off in order to record the entire unidirectional solidification process. The measurements showed that the initial temperature (superheat) ranged from 1353.2 K to 933.6 K in all the experiments. With this experimental setup unidirectional heat flow was achieved and also convection associated with the pouring of the liquid into the mould was eliminated.

After directional solidification, the cylindrical ingots were cut on a mid longitudinal plane. Then, the samples were polished with sand paper and etched with 1: 1: 1 HCl / HNO₃ / H₂O. Etching was performed at room temperature [20]. The position of the transition was located by visual observation and optical microscopy, and the distance from the bottom of the sample was measured with a ruler, see Figure 2.

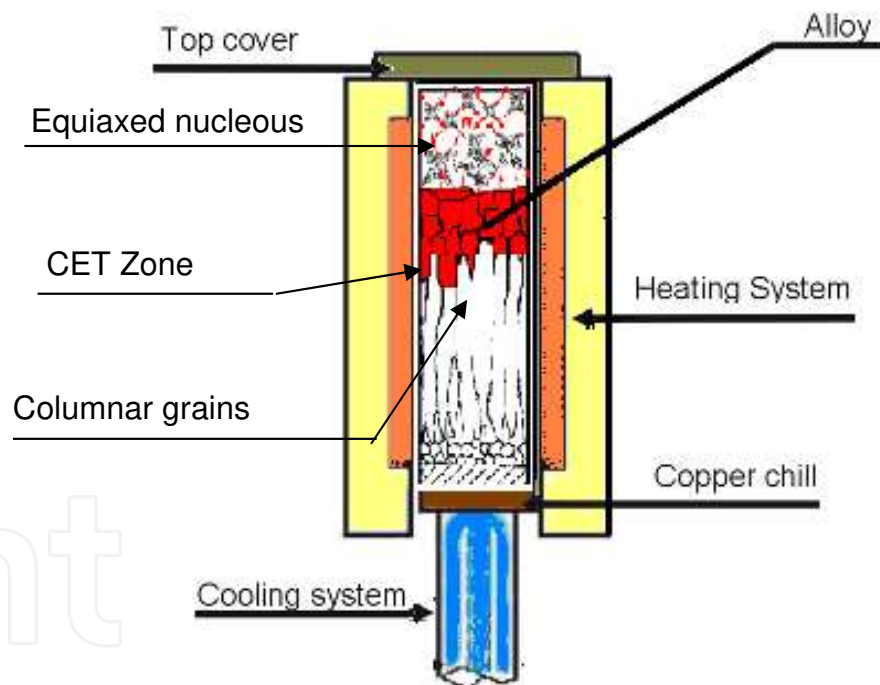


Figure 1. Schematic of experimental device for directional solidification tests.

The microstructure was analyzed using Scanning Electron Microscopy (SEM) and an inverted metallographic microscope (Arcano XTL 3400). Utilizing ASTM E112 standard norm and a typical histogram showing the frequency of the size of the equiaxed grains for each sample, the equiaxed grain size was measured, at equally spaced intervals, the counting starts at the position where the transition begun. The columnar region was divided in similar way and the width and length of the grains measured directly (Ares et al., 2007, 2010).

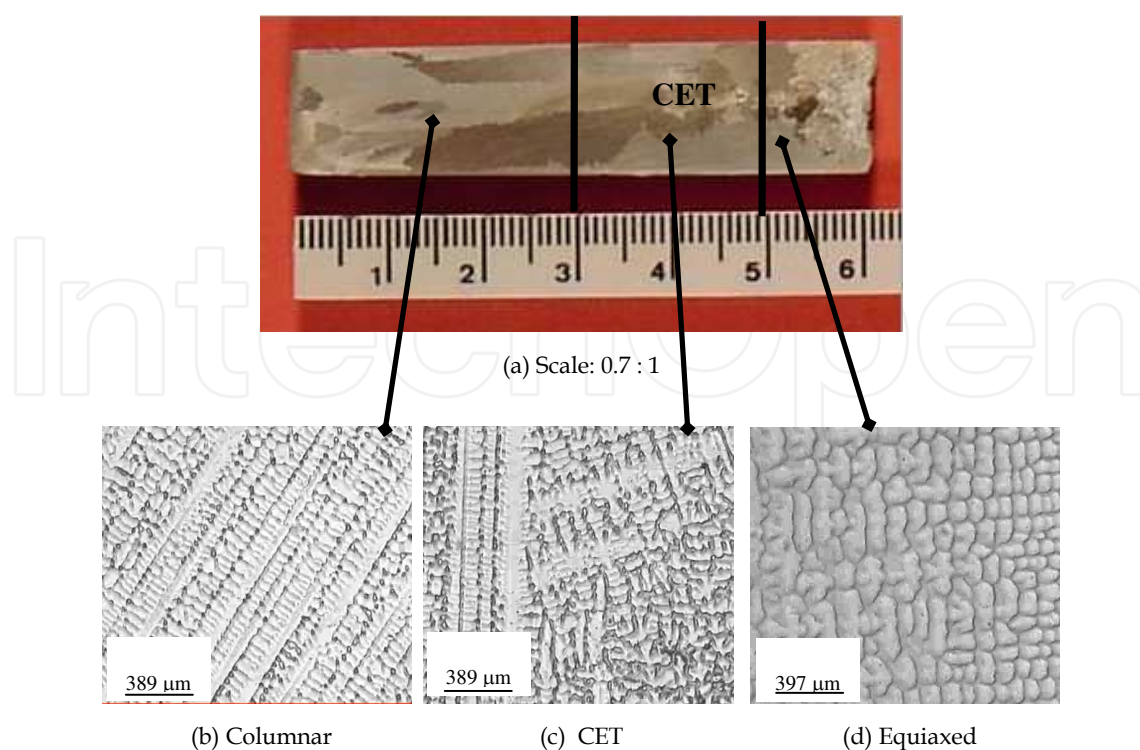


Figure 2. Obtained structures during directional solidification of 316 L stainless steel. (a) Macrostructure. (b-d) Representative microstructures in columnar, CET and equiaxed zones of the samples.

For measuring the secondary dendritic spacing, λ_2 , samples were again grounded and polished until a mirror finish. Etching was performed to reveal the microstructure, which was observed by an optical microscope. With the help of TSVIEW® image processing program, the secondary dendritic spacing value, λ_2 , was obtained for each sample, averaging 15 measures in each zone of the samples.

3. Electrochemical tests

For the electrochemical tests, samples of 20 mm in length of each zone and for each concentration were prepared as test electrodes (see Figure 3), polished with sandpaper (from SiC # 80 until # 1200) and washed with distilled water and dried by natural flow of air. Table 2 shows the compositions used for analysis.

All the electrochemical tests were conducted in 3wt% NaCl solution (pH = 5.5) at room temperature using an IM6d Zahner®-Elektrik potentiostat coupled to a frequency analyzer system. Oxygen was removed from the 3% solution of NaCl in the cell by a stream of nitrogen.

A conventional three-compartment glass electrochemical cell with its compartments separated by ceramic diaphragms was used. The test electrodes consisted of sections of the ZA ingots (see Figure 3) were positioned at the glass corrosion cell kit (leaving a rectangular area in

Element	Sample					
	A (316)	B (316L)	C (316L)	D (316L)	E (316L)	F (316)
C	0.08	0.03	0.03	0.03	0.03	0.08
Si	1.00	1.00	1.00	1.00	1.00	1.00
Mn	2.00	2.00	2.00	0.50	2.00	2.00
P	0.045	0.045	0.045	0.045	0.045	0.045
S	0.030	0.030	0.030	0.030	0.030	0.030
Cr	18.00	18.00	18.00	18.00	18.00	18.00
Ni	10.00	14.00	14.00	14.00	22.00	10.00
Mo	2.00	3.00	8.00	3.00	3.00	8.00
Fe	Balance	Balance	Balance	Balance	Balance	Balance

Table 2. Composition of the samples (weight percent)

contact with the electrolyte). The potential of the test electrode was measured against a saturated calomel reference electrode (0.242 V vs NHE), provided with a Luggin capillary tip. The Pt sheet was used as a counter electrode.

Impedance spectra were obtained in the frequency range of 10^{-3} Hz and 10^5 Hz at open circuit potential.

For comparison purposes, experiments with different structures were conducted under the same experimental conditions. All the corrosion tests experiments were triplicate and the average values and graphical outputs are reported.

The corrosion resistance of the material under study was investigated by performing cyclic potentiodynamic polarization curves, according to ASTM G61-86.

The samples were pre-catodized during 3 minutes at a potential of -1000 mV, lower than the open circuit potential. After that time the specimen was left open circuit for an hour, recording the open circuit potential. The scanning of the polarization curve began from the open circuit potential to more anodic potential at a rate of 0.1666 mV / s. When the current reached 5 mA/cm², the effect on the potentiodynamic polarization was reversed, continuing until the line intersects the curve outward, closing the hysteresis loop, or until it reaches the corrosion potential. The above procedure was performed for each obtained sample.

After completion the polarization tests, the samples were examined using Arcano® metallographic microscope.

In corrosion studies using EIE technique, the obtained impedance spectra are usually analyzed using electrical circuits composed by components such as resistance (R), capacitance (C), inductance (L), etc., combined all to reproduce the measured impedance spectra. These circuits are called "equivalent circuit" (Ferreira & Dawson, 1985).

The equivalent circuit shown in Figure 4 was proposed, where R_{Ω} corresponds to the resistance of the electrolyte, R_1 corresponds to the resistance to charge transfer, R_2 accompanies the double

layer and is referred to the resistance of the oxide layer; capacitances C come from the constant phase elements: C_1 values are attributed to the ability of the double layer and C_2 correspond to porous oxides capabilities (Polo et al., 1999).

To carry out the measurements, all samples were sanded CSi gradation # 1500, the assays were performed under constant nitrogen bubbling.

The test conditions were as follows:

- At -1000 mV during 3 minutes:
- Open circuit for 1 hour
- Potential amplitude: 10 mV/s around the open circuit potential
- Frequency range: 100 kHz to 1 mHz
- Points / decade: 10
- Stabilization of the system: 600 seconds

The measurements were performed at open circuit potential. For adjustment of the results we used the method of nonlinear least squares designed by Bouckamp (Winston Revie, 2000). We worked with a Gamry EIS Instrument, in combination with the LYP M7 potentiostat.

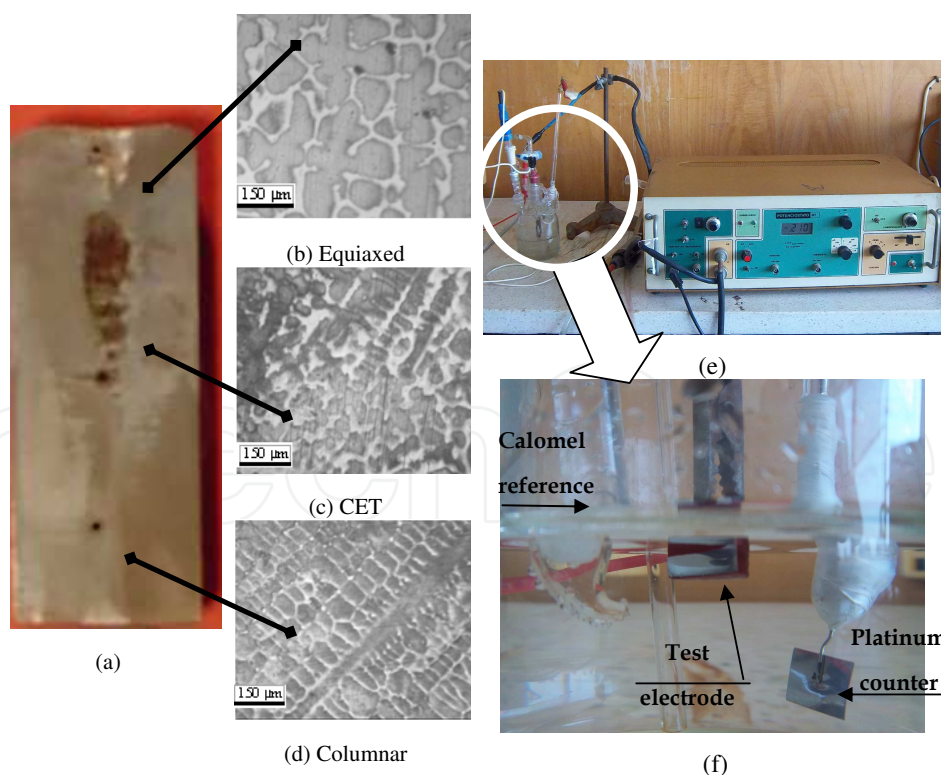


Figure 3. (a) Macrostructure. (b) to (d) Structures of work electrodes (columnar, CET and equiaxed). (e) Experimental device for electrochemical tests. (f) A glass corrosion cell kit with a platinum counter electrode and a Calomel reference electrode (SCE).

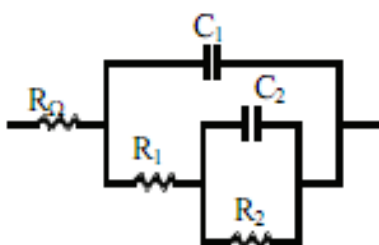


Figure 4. Proposed equivalent circuit.

4. Cyclic potentiodynamic polarization curves

Figure 3 shows the polarization curves obtained in 3% NaCl solution for one of the samples.

Localized corrosion was strongly influenced by the alloy composition, comparing the difference between the corrosion potential and the pitting potential in the same test, positioned longitudinally and then transversely to the reference electrode. It was observed that the samples for the group of 316 steels showed higher values than those found for samples of 316L stainless steel, they demonstrated that the potential start of pitting close to 1000 mV, while those rarely exceeded 500 mV at pitting potential (Figure 5).

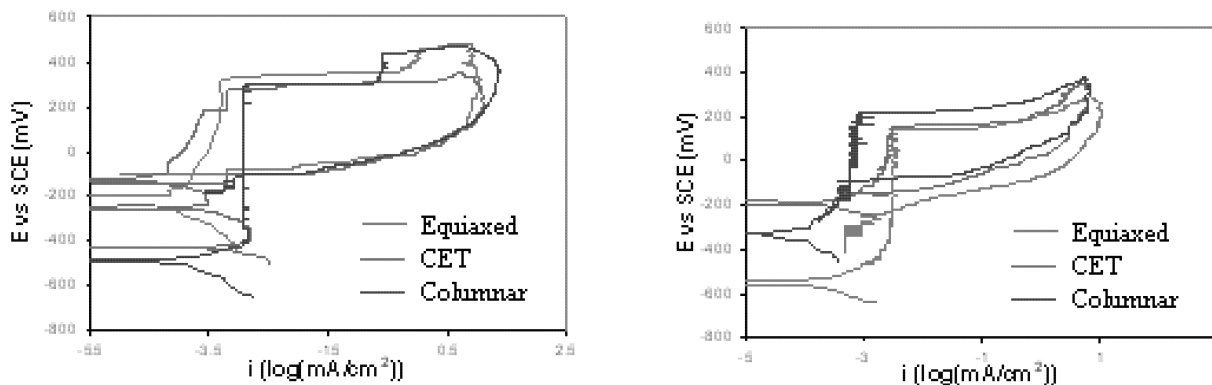


Figure 5. Cyclic potentiodynamic polarization curves of E sample, in 3% NaCl, (a) longitudinally and (b) transversally positioned, with respect to the reference electrode.

Once the process of pits formation started, evidenced by a sharp increase in the current density with respect to the potential, the specimen that turned to passivity almost immediately achieved after reversing the direction of the polarization was the specimen belonging to the group 316 stainless steels containing molybdenum in greater proportion. The other suffered bites that could not passivated again completely. As an example, in Figure 6 it is possible to observe the pits having one specimen.

The lower carbon content alloys were provided in some areas of passivity defined.

In Table 3 can be seen the various corrosion parameters of the analyzed samples.

	Sample	Corrosion	Pitting	Repassivation	$E_{pic} - E_{corr}$	$E_{pic} - E_{rep}$	$E_{rep} - E_{corr}$	
		Potential, E_{corr}	Potential, E_{pic}	potential , E_{rep}				
F	Long	equiaxed	-131	932	915	1063	17	1046
		CET	-540	845	833	1385	12	1373
		columnar	-170	923	328	1093	595	498
	Trans	equiaxed	-312	891	878	1203	13	1190
		CET	-437	885	876	1322	9	1313
		columnar	-552	942	-252	1494	1194	300
B	Long	equiaxed	-580	246	-86	826	332	494
		CET	-501	443	-135	944	578	366
		columnar	-488	441	-123	929	564	365
	Trans	equiaxed	-560	121	-23	681	144	537
		CET	-563	76	-9	639	85	554
		columnar	-290	464	-348	754	812	-58
E	Long	equiaxed	-222	322	-72	544	394	150
		CET	-429	271	142	700	129	571
		columnar	-486	292	-114	778	406	372
	Trans	equiaxed	-556	140	-229	696	369	327
		CET	-196	157	-146	353	303	50
		columnar	-330	220	-113	550	333	217
C	Long	equiaxed	-504	324	-215	828	539	289
		CET	-568	250	-224	818	474	344
		columnar	-673	359	-168	1032	527	505
	Trans	equiaxed	-436	193	-206	629	399	230
		CET	-503	158	-176	661	334	327
		columnar	-583	81	-262	664	343	321
D	Long	equiaxed	-123	334	-163	457	497	-40
		CET	-208	278	-259	486	537	-51
		columnar	-184	162	-311	346	473	-127
	Trans	equiaxed	-65	495	-98	560	593	-33
		CET	-232	569	-330	801	899	-98

Sample	Corrosion	Pitting	Repassivation	$E_{pic} - E_{corr}$	$E_{pic} - E_{rep}$	$E_{rep} - E_{corr}$	
	Potential, E_{corr}	Potential, E_{pic}	potential, E_{rep}				
columnar	-195	296	-244	491	540	-49	
equiaxed	-366	1006	-161	1372	1167	205	
A Long	CET	904	-25	1034	929	105	
	columnar	-120	911	-191	1031	1102	-71
A Trans	equiaxed	-71	991	-116	1062	1107	-45
	CET	-259	906	906	1165	0	1165
	columnar	-246	996		1242		

Table 3. Potential values found in the studied samples (mV).

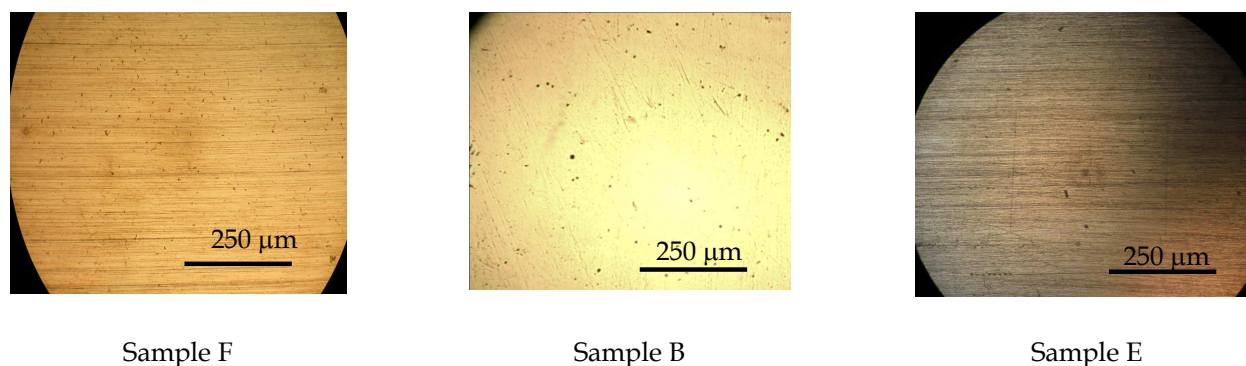


Figure 6. Surface of the samples after being subjected to cyclic potentiodynamic polarization testing in 3% solution of NaCl (magnification 100x).

5. Electrochemical Impedance Spectroscopy (EIE)

EIE measurements were performed at open circuit potential, or the potential for corrosion, because all the samples without exception have become passives at this potential. Therefore, the obtained results, corresponds to the behaviour of the passive layer formed.

Figure 7 shows the Bode and Nyquist obtained for one of the alloys studied, it can be observed a good agreement between experimental and simulated data. Table 4 lists the values found on the parameters used in the simulation.

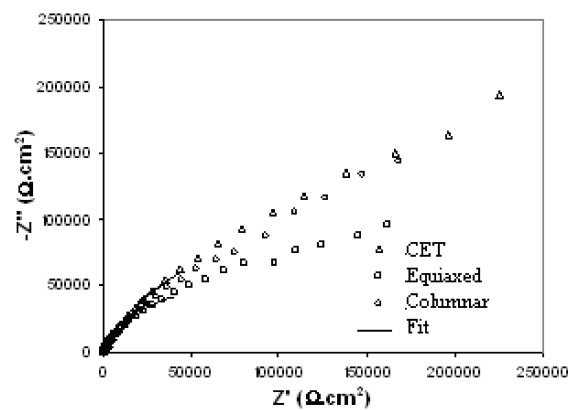
Impedance diagrams represented in a Nyquist diagram for all compositions showed similar shapes to each other, show a depression below the real axis. This flattening may be due to improper cell design, surface roughness or surface porosity.

From these tests it was observed that the porosity of the passive layer formed on the metal surface was variable, being more compact in areas with equiaxed structure in some alloys, and

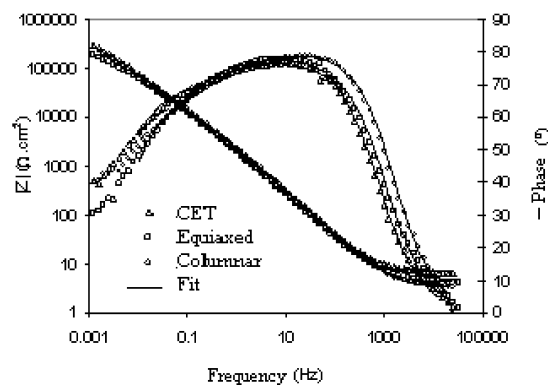
in areas with columnar structure, in others. Passive film 316L alloy with 8% Mo was, in general, the less porous the compositions studied, being therefore a protective oxide layer. This is consistent with the polarization tests conducted in which this alloy had a good performance against pitting corrosion within the group of 316L stainless steel. The other samples showed more or less compact films, depending on the type of structure in question, as noted above. The degree of porosity of the passive layer, given by the values of n_2 [9], can influence the behavior of the alloy against pitting corrosion, whose study exceeds the limits of this work.

The resistance of formed oxides related to the parameter R_2 , also had a variable behaviour, depending largely on the type of solidification structure, and the alloy composition. In this type of testing could not be establishing a clear relationship between the content of alloying elements in the metal and their behaviour. However, the oxide layers formed more resistant in certain areas of the samples, mostly those with columnar grains and with CET, were not necessarily the most compact.

One example is found in the area of one of the columnar steel samples 316, which showed resistance values the oxide layer by an order of magnitude greater than the other, with a medium to high porosity. Said alloy, corresponding to the composition of 0.08% C and 2% Mo, chopped reached potentials which were around 1000 mV, but without passivation capability.



(a)



(b)

Figure 7. Diagrams obtained by EIS tests for sample B: (a) Nyquist diagrams and (b) Bode diagrams.

Parameter	Sample								
	C			D			A		
	Columnar	CET	Equiaxed	Columnar	CET	Equiaxed	Columnar	CET	Equiaxed
R_{Ω} ($\Omega \text{ cm}^2$)	5.46	3.30	3.84	6.00	4.17	3.56	4.83	3.45	3.28
C_1 (μFcm^{-2})	52.26	102.47	48.51	89.38	58.63	48.86	26.54	59.74	53.34
n_1	0.91	0.88	0.91	0.88	0.88	0.90	0.88	0.91	0.89
R_1 ($\text{k}\Omega\text{cm}^2$)	195.04	17.17	48.32	98.88	10.08	35.01	19.78	20.23	40.62
R_2 ($\text{k}\Omega \text{ cm}^2$)	507.74	77.11	208.51	452.16	488.99	317.10	1347.50	168.92	603.60
C_2 (μFcm^{-2})	33.77	78.48	22.12	27.50	29.39	31.08	9.11	31.63	27.90
n_2	0.79	0.64	0.70	0.67	0.58	0.61	0.58	0.63	0.82
χ^2	1.10^{-3}	1.10^{-3}	1.10^{-3}	1.10^{-3}	1.10^{-3}	1.10^{-3}	1.10^{-3}	1.10^{-3}	1.10^{-3}

Parameter	Sample								
	F			B			E		
	Columnar	CET	Equiaxed	Columnar	CET	Equiaxed	Columnar	CET	Equiaxed
R_{Ω} ($\Omega \text{ cm}^2$)	5.18	4.38	3.18	3.39	6.66	4.38	4.57	4.72	4.94
C_1 (μFcm^{-2})	45.67	70.47	103.37	74.00	91.70	104.07	67.27	101.88	55.20
n_1	0.87	0.90	0.86	0.90	0.87	0.87	0.87	0.88	0.90
R_1 ($\text{k}\Omega \text{ cm}^2$)	10.25	10.20	3.30	8.81	30.51	38.08	22.30	6.67	14.53
R_2 ($\text{k}\Omega \text{ cm}^2$)	326.31	145.91	35.30	15.41	189.82	84.68	403.28	116.04	348.93
C_2 (μFcm^{-2})	46.74	62.31	126.72	36.60	34.55	73.40	21.63	165.06	23.88
n_2	0.55	0.61	0.53	0.60	0.73	0.80	0.62	0.66	0.66
χ^2	1.10^{-3}	1.10^{-3}	1.10^{-3}	1.10^{-3}	1.10^{-3}	1.10^{-3}	1.10^{-3}	1.10^{-3}	1.10^{-3}

Table 4. Setting parameters of the EIS simulation at the corrosion potential.

6. Microstructure: Secondary dendritic arm spacing

In Figure 8 it is possible to observe the measurements of secondary dendritic arm spacings, λ_2 , along the samples.

The values of secondary dendritic spacing, λ_2 , obtained from the micrographs were plotted as a function of the distance from the base of the sample (Figure 9), following the order: columnar, CET and equiaxed zones, the average values in each zone are summarized in Table 5. The values of λ_2 obtained for 316 steels were 20 μm below the values of λ_2 for 316L steels, but in all the samples, values of λ_2 in the zones of the samples with columnar solidification structure were lower than those found in zones with equiaxed structure. The values of measurements in the CET zones were variable, being intermediate between columnar and equiaxed zones in some cases, or resulting the lower values from the three structures in others cases.

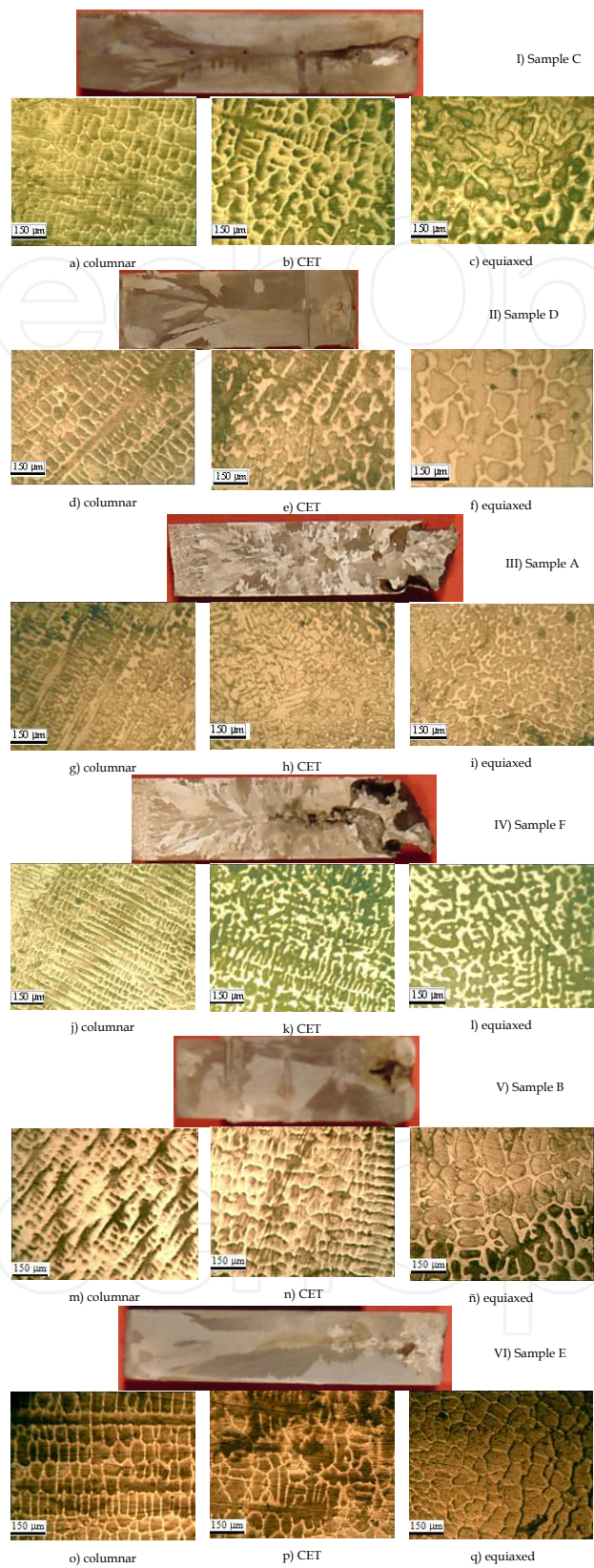


Figure 8. Solidification structures of 316 L. I-VI) Macrostructures; a-q) Microstructures.

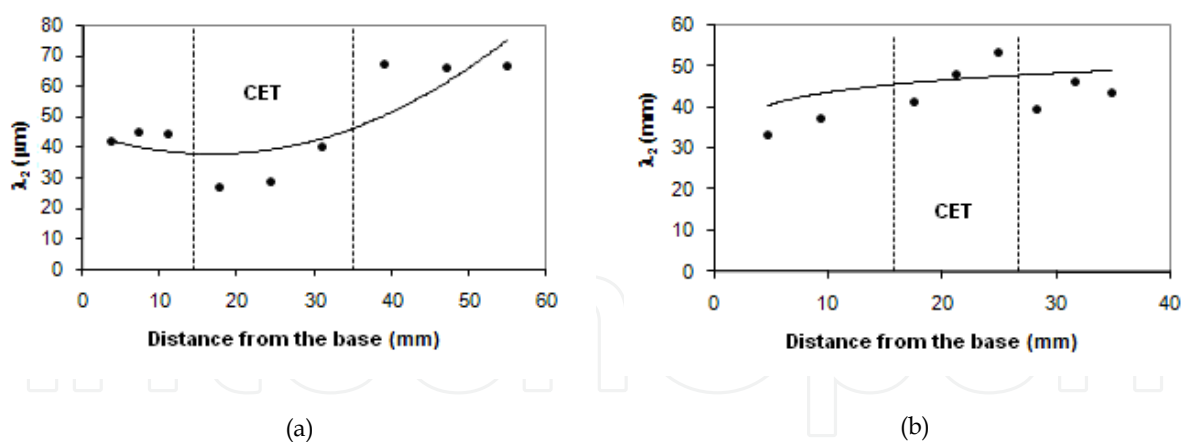


Figure 9. Secondary dendritic arm spacings versus distance, for 316 L samples: (a) Sample C and (b) Sample B.

		Sample					
		C	D	A	F	B	E
Secondary dendritic arm spacing, λ_2 (μm)	Columnar	43.57	66.40	29.85	26.51	48.20	50.73
	CET	31.75	49.96	41.14	34.65	47.59	58.79
	Equiaxed	66.37	74.21	42.86	38.53	43.04	60.28

Table 5. Averages values of secondary dendritic arm spacings for each sample.

7. Summary

Present knowledge about resistance to corrosion and passivity of 316L stainless steel directionally solidified samples is limited. This is the complex problem and it is necessary to deal with it as the separate question in the analysis of microstructure evolution and electrochemical properties of the stainless steels.

Alloys corresponding to stainless steels 316 L group presented passivity in defined zones and with varying of re-passivation, while 316 stainless steels began to pitting corrosion at much higher potentials.

In general, 316 steel samples with higher content of Mo were the more resistant to pitting corrosion, in zones corresponding to equiaxed and CET solidification structures.

Molybdenum content in the alloys was beneficial, promoting re-passivation in samples that containing a higher proportion of this element.

The oxide layer formed on the stainless steel corresponding to Sample C was one of the less porous and with higher values of the transfer of charge resistance, while Sample A, formed a protective passive film in the columnar zone but with very low charge-transfer-resistance, and a high porosity, making it susceptible to localized corrosion.

Zones with equiaxed structure showed the highest values of secondary dendritic arm spacings within the same sample, and a good ability to re-passivation after pitting, while zones with columnar structure and with CET having passive zones larger than equiaxed structure.

The steel of Sample F had the best performance against located corrosion, while Sample D was the most susceptible to this type of attack.

Acknowledgements

One of the authors, Alicia Esther Ares, would like to thanks Consejo Nacional de Investigaciones Científicas y Técnicas (CONICET) from Argentina for the financial support.

Author details

Claudia Marcela Méndez¹, Mónica Mariela Covinich¹ and Alicia Esther Ares^{2*}

*Address all correspondence to: aares@fceqyn.unam.edu.ar

1 Materials Laboratory, Faculty of Sciences, National University of Misiones, Posadas, Argentina

2 Researcher from National Scientific and Technical Research Council, Argentina

References

- [1] Al-Fozan, S.A.; Malik, A. U. (2008) Effect of seawater level on corrosion behavior of different alloys, *Desalination*, Vol. 228, p.p. 61–67.
- [2] Ardakani, M.G.; D'Souza, N. ; Wagner, A.; Shollock, B.A.; McLean, M. (2000) Competitive Grain Growth and Texture Evolution during Directional Solidification of Superalloys, *Superalloys 2000*, Edited by T.M. Pollock, R.D. Kissinger, R.R. Bowman, K.A. Green, M. McLean, S. Olson, and J.J. Schirra, TMS (The Minerals, Metals & Materials Society).
- [3] Ares, A.E.; Schvezov, C.E. (2000) Solidification Parameters During the Columnar-to-Equiaxed Transition in Lead-Tin Alloys. *Metallurgical and Materials Transactions A*, Vol. 31, 1611-1625.
- [4] Ares, A.E.; Gueijman, S.F.; Schvezov, C.E. (2010) Experimental Study of the Columnar-to-Equiaxed Transition During Directional Solidification of Zinc-Aluminum Alloys and Composites, *J. Crystal Growth*, Vol. 312, pp. 2154-2170.

- [5] Ares, A.E.; Gueijman, S.F.; Caram, R.; C.E. Schvezov (2005) Analysis of Solidification Parameters During Solidification of Lead and Aluminum Base Alloys. *J. Crystal Growth*, Vol. 275, pp. 235-240.
- [6] Ares, A.E.; Schvezov, C.E. (2007) Influence of Solidification Thermal Parameters on the Columnar to Equiaxed Transition of Al-Zn and Zn-Al Alloys. *Metallurgical and Materials Transactions A*, Vol. 38, pp. 1485-1499.
- [7] Ares, A.E.; Gueijman, S.F.; Schvezov, C.E. (2002) Semi-Empirical Modeling for Columnar and Equiaxed Growth of Alloys. *J. Crystal Growth*, Vol. 241, pp. 235-240.
- [8] Azuma, S.; Kudo, T.; Miyuki, H.; Yamashita, M.; Uchida, H. (2004) Effect of nickel alloying on crevice corrosion resistance of stainless steels, *Corrosion Science*, Vol. 46, p.p. 2265–2280.
- [9] Batra, U., Ray, S., Prabhakar, S.R. (2003) Effect of austenitization on austempering of copper alloyed ductile iron. *J Mater Eng Perf.*, Vol. 12 (5): p.p. 597–601.
- [10] Cai, B.; Liu, Y.; Tian, X.; Wang, F.; Li, H.; Ji, R. (2010) An experimental study of crevice corrosion behaviour of 316L stainless steel in artificial seawater, *Corrosion Science*, Vol. 52, p.p. 3235-3242.
- [11] Chastain, S. (2004), *Metal casting: a sand casting manual for the small foundry*, Vol. II 4, Stephen Chastain, ISBN 978-0-9702203-3-2.
- [12] Chupatanakul, S., Nash, P. (2006) Dilatometric measurement of carbon enrichment in austenite during bainite transformation. *J Mater Sci.*, Vol. 41 (15): p.p. 4965–9.
- [13] DOD Technical Bulletin – Corrosion Prevention and Detection, Department of the Navy, United States of America.
- [14] Ferreira, M.G., Dawson, L.J. (1985) Electrochemical studies of the passive film of 316 stainless steel in chloride media, UMIST, Corrosion and Protection Centre, Manchester, England M60 1QD.
- [15] Freire, L.; Catarino, M.A.; Godinho, M.I.; Ferreira, M.J.; Ferreira, M.G.S.; Simões, A.M.P.; Montemor, M.F. (2012) Electrochemical and analytical investigation of passive films formed on stainless steels in alkaline media, *Cement & Concrete Composites* Vol. 34, p.p.1075–1081.
- [16] Freire, L.; Nóvoa, X.R.; Montemor, M.F.; Carmezim, M.J. (2009) Study of passive films formed on mild steel in alkaline media by the application of anodic potentials, *Materials Chemistry and Physics*, Vol. 114, p.p. 962–972.
- [17] Gäumann, M.; Bezençon, C.; Canalis, P. et al. (2001) Single-Crystal Laser Deposition of Superalloys: Processing-Microstructure Maps. *Acta Mater.*, Vol. 49, pp.1051-1062.

- [18] Hamdy, A.S.; El-Shenawy, V.; El-Bitar, T. (2006) Electrochemical Impedance Spectroscopy Study of the Corrosion Behavior of Some Niobium Bearing Stainless Steels in 3.5% NaCl, *Int. J. Electrochem. Sci.*, Vol. 1, p.p. 171-180.
- [19] Ilevbare, G.O. ; Burstein, G.T. (2001) The role of alloyed molybdenum in the inhibition of pitting corrosion in stainless steels, *Corrosion Science*, Vol. 43, p.p. 485-513.
- [20] Khalfallah, I.Y.; Rahoma, M.N.; Abboud, J.H.; Benyounis, K.Y. (2011) Microstructure and corrosion behavior of austenitic stainless steel treated with laser, *Optics & Laser Technology*, Vol. 43, p.p. 806–813.
- [21] Kilicli, V., Erdogan, M. (2008) The Strain-Hardening Behavior of Partially Austenitized and the Austempered Ductile Irons with Dual Matrix Structures. *J Mater Eng Perf.*, Vol. 17 (2), p.p. 240–249.
- [22] Lambers, H.G., Tschumak, S., Maier, H.J., Canadinc, D. (2009) Role of Austenitization and Pre-Deformation on the Kinetics of the Isothermal Bainitic Transformation. *Metal Mater Trans A*. Vol. 40 (6) p.p. 1355-1366.
- [23] Liou, H.Y.; Rong-Iuan Hsieh, R.I.; Tsai, W.T. (2002) Microstructure and stress corrosion cracking in simulated heat-affected zones of duplex stainless steels, *Corrosion Science*, Vol. 44, p.p. 2841–2856.
- [24] Machuca, L.L. ; Bailey, S.I. ; Gubner, R. (2012) Systematic study of the corrosion properties of selected high-resistance alloys in natural seawater, *Corrosion Science*, Vol. 64, p.p. 8–16.
- [25] McFadden, S.; Browne D.J.; Gandin C.A. (2009) A Comparison of Columnar-to-Equiaxed Transition Prediction Methods Using Simulation of the Growing Columnar Front. *Metall Mater Trans A*, Vol. 40, pp. 662-672.
- [26] Mottu, N.; Vayer, M.; Dudognon, J.; Erre, R. (2004) Structure and composition effects on pitting corrosion resistance of austenitic stainless steel after molybdenum ion implantation, *Surface & Coatings Technology*, Vol. 200, p.p. 2131– 2136.
- [27] Orazem, M. E., Tribollet, B. (2008) "Electrochemical Impedance Spectroscopy"; John Wiley and Sons, Inc.
- [28] Pardo, A., Merino, M.C., Coy, A.E., Viejo, F., Arrabal, R., Matykina, E. (2008) Pitting corrosion behaviour of austenitic stainless steels – combining effects of Mn and Mo additions, *Corrosion Science*, Vol. 50 p. p. 1796-1806.
- [29] Pardo, A.; Merino, M.C.; Coy, A.E.; Viejo, F.; Arrabal, R.; Matykina, E. (2008) Effect of Mo and Mn additions on the corrosion behaviour of AISI 304 and 316 stainless steels in H₂SO₄, *Corrosion Science*, Vol. 50, p.p. 780–794.
- [30] Park, K.; Kwon, H.S. (2010) Effects of Mn on the localized corrosion behavior of Fe–18Cr alloys, *Electrochimica Acta* Vol. 55, p.p. 3421–3427.

- [31] Polo, J. L., Torres, C. L., Cano, E., Bastidas, J. M. (1999) Estudio de impedancia de la corrosión del acero inoxidable AISI 316L en las regiones pasiva y de picadura, *Revista de Metalurgia*, Vol. 35, p. 368-378.
- [32] Polo, J.L. ; Cano, E. , Bastidas, J.M. (2002) An impedance study on the influence of molybdenum in stainless steel pitting corrosion, *Journal of Electroanalytical Chemistry*, Vol. 537, p.p. 183-187.
- [33] Pisareka, M.; Kędzierzawskib, P.; Płociński, T.; Janik-Czachor, M.; Kurzydłowski, K.J. (2008) Characterization of the effects of hydrostatic extrusion on grain size, surface composition and the corrosion resistance of austenitic stainless steels, *Materials Characterization*, Vol. 59, p.p. 1292-1300.
- [34] Reinhart G.; Mangelinck-Noël N.; Nguyen-Thi H.; Schenk T.; Gastaldi J.; Billia B.; Pino P.; Härtwig J.; Baruchel J. (2005) Investigation of Columnar–Equiaxed Transition and Equiaxed Growth of Aluminium Based Alloys by X-ray Radiography. *Mater Sci Eng A*, Vol. 413–414, pp. 384–388.
- [35] Spittle J.A. (2006) Columnar to Equiaxed Grain Transition in as Solidified Alloys, *International Materials Reviews*, Vol.51, No.4, pp. 247–269.
- [36] Stefanescu, D.M. (2008), *Science and Engineering of Casting Solidification* (2nd ed.), Springer, ISBN 978-0-387-74609-8.
- [37] Winston Revie, R. (2000) *Uhlig’s Corrosion Handbook, Austenitic and Ferritic Stainless Steels*, 2° ed., EE.UU., p. 601-628.

